geopress.

# Modeling the Ionosphere-Thermosphere System

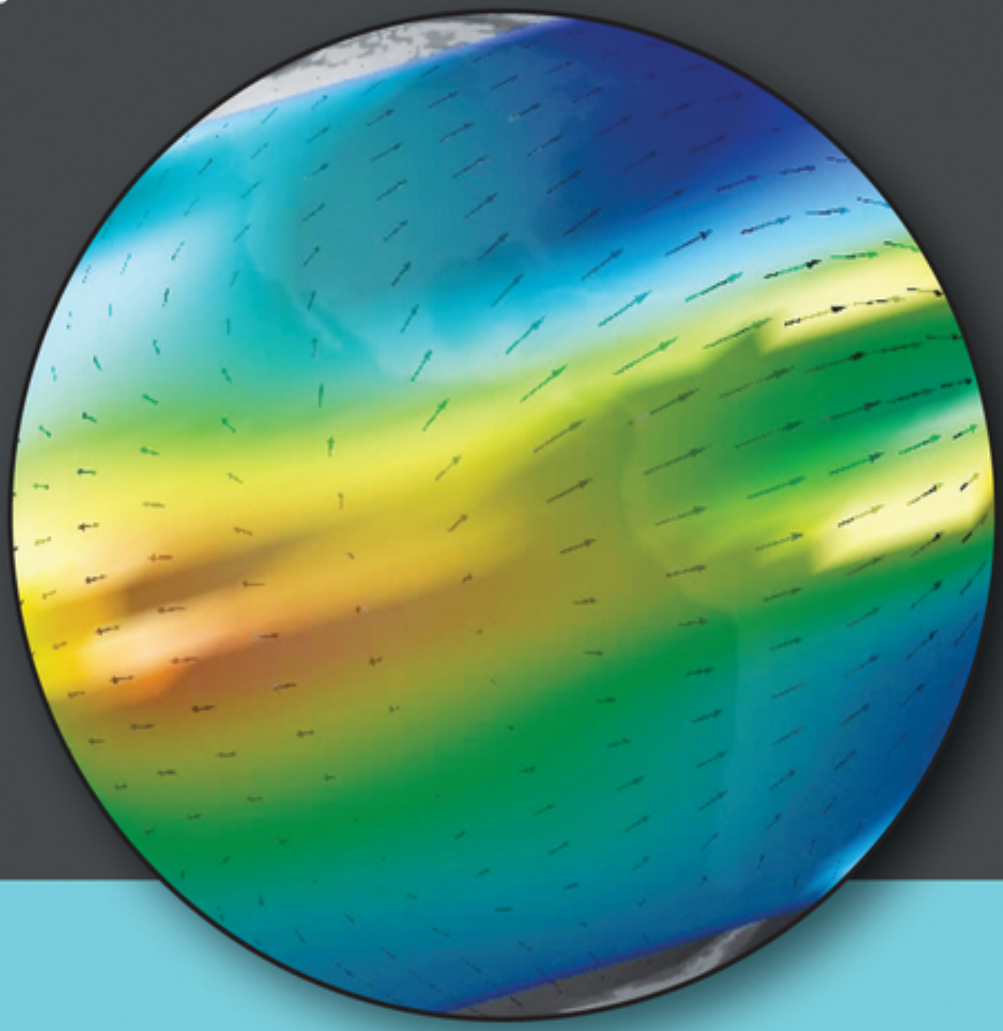

*J.D. Huba, R.W. Schunk, and G.V. Khazanov*
*Editors*

AGU
American Geophysical Union

# CONTENTS

# List of Tables

# List of Illustrations

km) heat flux of —1 × $10_{10}$ eV $cm^{-2}$ $s^{-1}$ was used for these simulations to account for the interaction of the ionospheric electrons with the hot polar rain electrons. From Schunk et al. [1987].

Figure 3. Ion density profiles calculated for a daytime high-latitude ionosphere subjected to a 100 mV $m^{-1}$ electric field. The curves labeled 2 were calculated with $T_i$, and the curves labeled 1 were calculated with $T_{i\|}$. From *Schunk et al.* [1975].

Figure 4. (top) Altitude profiles of the adopted electron, ion, and neutral temperatures used in subauroral red (SAR) arc calculations; $T_e(1)$ and $T_e(2)$ are the electron temperatures outside and inside the SAR arc, respectively. (bottom) Calculated ion and electron density profiles in a SAR arc including the effect of $N_2$ vibrational excitation and the associated increase in the $O^+ + N_2 \Rightarrow NO^+ + N$ reaction. From *Raitt et al.* [1976].

Figure 5. Proton heat flows along **B** for the transport of parallel energy ($q_p^{\|}$), perpendicular energy ($q_p^{\perp}$), and total energy ($q_p$) along a SAR arc field line, where $q_p = (q_p^{\|} + 2q_p^{\perp})/2$. Solid curves correspond to the solution of the 16-moment bi-Maxwellian transport equations. The dashed curve is not relevant to the discussion in the paper. From *Demars and Schunk* [1986].

Figure 6. Electron density as a function of dipole latitude for the (a) single-stream $H^+$ model and for the (b) two-stream $H^+$ model. The multiple curves show the temporal evolution of the electron density as the flux tube fills, with the 0 min curves corresponding to the start of the simulations. From Rasmussen and Schunk [1988].

Figure 7a. Effect of multiple propagating plasma patches on the thermosphere at $t$ = 3 h. (left top) The $N_e$ distribution at 300 km in units of $\log_{10} N_e$ ($cm^{-3}$), (right top) the neutral density perturbation at 300 km, and (bottom) the neutral density perturbation versus altitude and latitude across the polar cap. From *Ma and Schunk* [2001].

Figure 7b. Snapshot at $t$ = 4.41 h of the neutral density perturbation due to multiple propagating plasma patches. The neutral perturbation is shown (left) at 300 km and (right) as a function of altitude and latitude across the polar cap. From *Schunk et al.* [2008].

Chapter 02

Figure 1. Typical global distribution of some of the major model parameters at the December solstice at moderate solar and geomagnetic activity, (left top) The contours of neutral temperature and total wind vector and (right top) the contours of meridional wind on a fixed pressure level in the upper thermosphere close to 300 km. (left bottom) Neutral density at a fixed altitude of 300 km and (right bottom) the height-integrated 0/N2 ratio (figure courtesy of Mariangel Fedrizzi, 2012).

Figure 2. Illustration of the change in the neutral wind at midlatitude and low latitudes at 250 km altitude shortly after a sudden increase in the high-latitude magnetospheric energy input. The region within 50° of the geographic equator is shown at 15 UT, 3 h after the increase in the high-latitude magnetospheric forcing, equivalent to a Kp ~7.

Figure 3. Illustration of the response of the thermosphere to heating and thermal expansion

(figure courtesy of Karen O'Loughlin, 2012).

Figure 4. Illustration of the response and evolution of a composition “bulge” in the summer hemisphere upper thermosphere in response to a 12 h geomagnetic storm from 10° latitude to the pole. The response is followed through 36 h of recovery. The figure shows the increase in mean molecular mass in atomic mass units, compared to a background simulation without a storm, on a fixed pressure level in the upper thermosphere around 300 km altitude, from 10° latitude to the pole.

Figure 5. Illustration of the response to elevated geomagnetic activity (Kp~7) of (left) neutral wind and temperature and (right) neutral density. The region poleward of 50° latitude is shown at 200 km altitude.

Figure 6. Illustration of the direction of forces for vortices driven by ion drag in the (left) clockwise and (right) counterclockwise direction. The forces are shown in a “natural” vortex coordinate system as suggested by Holton [1972].

Chapter 03

Figure 1. Schematic representation of the major processes in the ion chemistry of the Earth’s ionosphere based on the work of Richards [2011]. The circles represent the major neutral species, the boxes represent the important ions, and the arrows with labels show the various reactions and ionization processes. Photoelectron impact ionization is labeled e*, photoionization is labeled hv, and spontaneous radiation is labeled rad. The chemical reactions are labeled with the reacting species.

Figure 2. Model neutral densities for 5 September 2005 (full lines) and 17 March 1990 (broken lines).

Figure 3. Modeled ion densities (lines) for 6 September 2005 and 17 March 1990. The symbols are the measured ion densities.

Figure 4. O+(4S) production (solid lines) and loss (broken lines) rates for 6 September 2005 and 17 March 1990. The sources and sinks are labeled with the reacting species. Photoionization is labeled hv and photoelectron impact ionization is labeled e*.

Figure 5. O+(2D) production (solid lines) and loss (broken lines) rates for 6 September 2005 and 17 March 1990. The sources and sinks are labeled with the reacting species. Photoionization is labeled hv, and photoelectron impact ionization is labeled e*.

Figure 6. O+(2P) production (solid lines) and loss (broken lines) rates for 6 September 2005 and 17 March 1990. The sources and sinks are labeled with the reacting species. Photoionization is labeled hv, and photoelectron impact ionization is labeled e*.

Figure 7. production (solid lines) and loss (broken lines) rates for 6 September 2005 and 17 March 1990. The sources and sinks are labeled with the reacting species. Photoionization is labeled hv, and photoelectron impact ionization is labeled e*.

Figure 8. production (solid lines) and loss (broken lines) rates for 6 September 2005 and 17 March 1990. The sources and sinks are labeled with the reacting species. Photoionization is labeled hv, and photoelectron impact ionization is labeled e*.

Figure 9. NO+ production (solid lines) and loss (broken lines) rates for 6 September 2005 and 17

Figure 2. Hydrogen ion density as a function altitude at time 13:25 LT on day 4: semi-implicit (black) and fully implicit (red). Here the higher-density profile is in the Southern Hemisphere, and the lower-density profile is in the Northern Hemisphere.

Figure 3. Hydrogen ion velocity as a function altitude at time 13:25 LT on day 4: semi-implicit (black) and fully-implicit (red). Here the negative velocity profile is in the Southern Hemisphere, and the positive velocity profile is in the Northern Hemisphere.

Figure 4. Schematic of “flux tube” motion in the Lagrangian scheme.

Chapter 06

Figure 1. (top) Electric potential and (bottom) hemispherical average of upward current at the top of the ionosphere on 21 December, 4 UT, with 30 kV cross-polar cap potential drop, with no wind dynamo electric field source. (left) Case A does not use equivalent magnetospheric conductances; (right) case B does. The outer circles are 50° magnetic latitude, with magnetic local time shown.

Figure 2. Thermosphere-ionosphere-electrodynamics general circulation model (TIE-GCM) simulations of magnetic eastward current density as a function of magnetic latitude and height, for March equinox, 12 UT, 14 magnetic local time(approximately 30° geographic longitude), F10.7 = (left) Due to gravity and associated electric field. (right) Due to plasma pressure gradient and associated electric field.

Figure 3. TIME-GCM simulation of upward E x B drift at 135 km above the geomagnetic equator at 12 UT due to neutral wind (Wind; long-dashed blue line), gravity and pressure-gradient current (Jpg, short-

dashed orange line), penetration electric field (PE, dashed- dotted red line), and the sum of all sources (All, solid green line). Shown for comparison is the Scherliess/Fejer empirical model [Scherliess and Fejer, 1999] (thin purple double-dotted line) (figure reproduced from Maute et al. [2012]).

Figure 4. (opposite) (left) TIE-GCM simulation of ionospheric currents and (right) geomagnetic perturbations as a function of magnetic local time and magnetic latitude for solar minimum, 8 June, 17 UT (when the subsolar point is at its northernmost magnetic latitude). For currents, arrows show the height-integrated sheet current density, K, and colors show the upward component of field-aligned current density at the top of the current sheet, Jqr. For magnetic perturbations, arrows show the horizontal components and, colors, the vertical component (positive downward). (top left) The total density, (middle left) the residual current, and (bottom left) the equivalent current. See main text for definitions of residual and equivalent currents. (top right) Magnetic perturbations at 400 km altitude due to equivalent current and (middle right) residual current, and (bottom left) magnetic perturbations at the ground, which by definition are due only to the equivalent current.

Chapter 07

Figure 1. (a) Data-model comparison of thermospheric neutral density at satellite perigees for satellite #12388 from 2002 to 2008. Black, satellite drag-derived density; red: thermosphere-ionosphere-electrodynamics general circulation model (TIE-GCM) simulation. (b) Corresponding F10.7 and Ap indices. Satellite #12388 (Cosmos

1236) has moderately eccentric orbits with perigees varying between 385 and 415 km and apogees varying between 1448 and 1585 km. The satellite perigees precess in latitude and LT, with approximately three latitude cycles and five local time cycles in a year.

Figure 2. Global NO cooling power, integrated over the globe and in the altitude range from 100 to 200 km, from 2002 to 2006. Black, TIMED/SABER; red, TIE-GCM simulation. The estimated uncertainty of SABER NO cooling rates is ~15% (adapted from the work of Qian et al. [2010a]).

Figure 3. NmF2 observed by Constellation Observing System for Meteorology Ionosphere and Climate, estimated by the International Reference Ionosphere, and simulated by TIE-GCM, during 2008. NmF2 is averaged over 10:00–13:00 LT and over the months shown in each panel.

Figure 4. Electron density profiles observed by Millstone Hill incoherent scatter radar (ISR), calculated by the ISR ionospheric model, and simulated by the TIE-GCM, at 12:00 and 15:00 LT, on 30 March 2007 and 21 June 2007.

Chapter 08

Figure 1. Temporal variation of (top) interplanetary magnetic field Bz, (middle) CPCP and (bottom) hemispheric integrated Joule heating in the Southern Hemisphere.

Figure 2. Temporal variation of the distributions of (a) buoyancy acceleration (m s-2) and (b) vertical wind (m s-1) in the Southern Hemisphere at 300 km altitude. The outside ring is -40°, and the time is

indicated at the top of each distribution. (left) Dusk and (top) noon.

Figure 3. The time versus altitude distribution of (a) buoyancy acceleration (m s −2) and (b) vertical wind (m s −1) at 77.5°S, 22.5°E during 15 min, 1 h, and 2 h time intervals. The location has been shown in Figure 2a.

Figure 4. (a) The temporal variation of the altitudinal profiles of Joule heating per unit volume (W m−3) at (77.5°S; 22.5°E) for (left) case 1 and (right) case 2. The numbers and arrows attached to the color bars indicate the minimum and maximum values in the color contour. (top) The line plots show the variations at 300 km altitude, and (right) the numbers represent the average value of the corresponding line plots. (b) is the same as (a), except for the buoyancy acceleration (ms−2). The Joule heating (a) is plotted on a logarithmic scale, and the buoyancy acceleration (b) is plotted on a linear scale.

Figure 5. The same as Figure 4, except for the vertical velocity (m s –1) (a), and the percentage difference of neutral density compared with the value in the background case (b), respectively.

Figure 6. (opposite) (a) Neutral density (kg m−3) distribution at 130 km altitude at 07:00 UT in the Southern Hemisphere. The neutral wind velocity vectors are plotted out on top of the neutral density, and the outside ring is —40°C. (b) Neutral density (kg m−3) distribution at 300 km altitude at 07:00 UT in the Southern Hemisphere. The logarithmic scale has been used for (a) and (b). (c) The same as (b) except for the percentage difference of neutral density at 300 km compared with the background case.

Chapter 10

ionospheric/thermospheric composition, temperature, electric fields, and neutral winds are being validated against observations. Derived products include total electron content (TEC), NmF2, hmF2, and total mass density.

Figure 2. (a) Solar EUV irradiance from the NRL's Solar Spectral Irradiance (NRLSSI) 2C and 3C models. (b) Geomagnetic and solar indices during the WHI 2008 interval. Bz turned negative at the onset of a weak geomagnetic storm due to a corotating interaction region on day 85 (dashed vertical line).

Figure 3. Daily global mean TEC from 1 March through 16 April 2008 is shown for the International Global Navigation Satellite Systems (GNSS) Service (IGS) GPS-derived TEC maps along with that for several A Model of the Ionosphere (SAMI3) simulations.

Figure 4. Daily global mean TEC is shown for the SAMI3 simulation using NRLSSI2C EUV irradiances. The dashed line shows the case in which only the day-of-year was allowed to vary. The dot-dashed line shows the case in which only the Ap index is held constant. The long-dashed line shows the case in which neutral winds are turned off.

Figure 5. A 2 h global mean IGS TEC is shown for days 80–90 during WHI 2008. The 15 min global mean TEC for SAMI3 using the NRLSSI 3C model is also shown. On most days, there appears to be a 180° phase shift in the diurnal variation of TEC between the data and model.

Figure 6. TEC at 10, 18, and 22 UT on day 86 and 10 UT on day 87 during WHI 2008 for (top) IGS, (middle) SAMI3, and (bottom) SAMI-SC. On day 86 at 22 UT,

Figure 3. Observations of the ion temperature from DMSP just following sunrise show ion temperatures that differ by 500 K when the dominant ion changes from O+ to H+. This apparent change is due entirely to the ionospheric composition.

Figure 4. Observations of the electron temperature across the high-latitude region show departures from an expected baseline, estimated by the black line, that are indicative of heat input to the ionosphere. Knowledge of the heat flux at the top of the ionosphere is required to reconcile these measurements.

Figure 5. Measurements of the ion and neutral velocities from the Dynamics Explorer satellite show regions near 85, 100 s in the top panel where the ion-neutral velocity is very high. In these regions, the ion/electron density, shown in the third panel is decreased, and the time for coupling to the neutrals, shown in the lowest panel, is increased [after Killeen et al., 1984].

Figure 6. Observations of ion drift and precipitating electrons made from the DMSP satellite show a rapid subauroral flow in the absence of any large field-aligned current. This implies that the conductivity of the medium must behave in a manner that is similar to the drift itself (courtesy, P.C. Anderson).

Figure 7. Calculations of the ion number density variation produced by altitude gradients in the neutral wind show that the contribution of vertical drifts due to zonal winds perpendicular to B and vertical drifts due to meridional winds parallel to B are the same at about 130 km altitude [after Osterman et al., 1995].

Chapter 15

Figure 1. Summary of meteorological variability in January 2009 from the Navy Operational Global Atmospheric Prediction System-Advanced Level Physics High Altitude (NOGAPS-ALPHA) assimilation product of Eckermann et al. [2009]. This product is used to initialize a series of six hourly forecasts (see text).

Figure 2. Monthly mean zonal winds from the thermosphere ionosphere electrodynamics general circulation model (TIEGCM) for (a) a bottom boundary with migrating tides from the global-scale wind model (GSWM) model and a globally invariant temperature. (b) The same migrating tides as in (a) but with a time-independent, latitudinally varying zonal mean temperature and winds from NOGAPS-ALPHA and (c) the complete varying wind and temperature fields from the NOGAPS-ALPHA forecast model for January 2009.

Figure 3. Difference fields for the TIEGCM calculations shown in Figure 1. (a) The middle panel of Figure 1 minus the left-hand panel (zonal mean + GSWM — pure GSWM). (b) The right panel of Figure 1 minus the middle (full NOGAPS — (zonal mean + GSWM).

Figure 4. (top 4) Monthly averaged amplitudes of four tidal components for temperature and (bottom 4) zonal wind. The temperature amplitudes are in degrees K, the zonal wind amplitudes are in m s−1 The four components are diurnal westward wave 1, semidiurnal westward wave 2, terdiurnal westward wave 3, and diurnal eastward wave 3. See text for the specific definitions of diurnal, semidiurnal, and terdiurnal.

Figure 5. Comparison of monthly averaged latitudinally variation of four tidal components of temperature (T) and zonal wind (U) tides calculated by NOGAPS-ALPHA and the TIEGCM. The dashed curve in each panel is the particular tidal component calculated from the NOGAPS-ALPHA input to the TIEGCM bottom boundary at the Z = −7 log-pressure level. The dotted and solid curves in each panel are the tidal components taken from the TIEGCM T and U solution at the lowest midpoint level (Z = −6.75). The solid curves are from the case where the TIEGCM U and V fields at Z = −6.75 are nudged by NOGAPS; the dotted curves are from the case without nudging. See text for a definition of the TIEGCM pressure levels and their relationship to NOGAPS-ALPHA pressure levels.

Figure 6. Comparison of monthly averaged profiles of the four zonal wind tides for the two approaches to proscribing the TIEGCM bottom boundary discussed in Figure 5. The solid lines result from nudging the U and V fields; the dashed lines are from the case without nudging. For reference, the migrating tides from a GSWM December solstice solution are presented as the dotted lines. Each panel is an average over a different range of latitudes associated with the peak of the tide. (a) An average from 22.5°N to 32.5°N, (b) an average from 52.5°N to 62.5°N, (c) an average from 52.5°N to 62.5°N, and (d) from 7.5°S to 7.5°N.

Figure 7. Snapshot of zonal wind variation at Z = −3.75 (about 120 km) as a function of longitude at 12 UT for 37°N on 10 January (solid curve) and 24 January (dashed curve).

Figure 8. A 2-D spectrum of zonal wind variation for the same location as in Figure 7, for two 5 day intervals (a) for 10–14 January 2009, a 5 day period before the major sudden stratospheric warming, and (b) for 20–24 January 2009, during the warming. The contours are in intervals of 5 m s−1 the peak magnitude of the large blotch at wave 2, 2 cycles d−1 in (a) is 40.5 m s-1

Chapter 16

Figure 1. Temperature at 90°N and lOh Pa of (a) January of the first year, (b) first year, and (c) 20 years of Whole Atmosphere Community Climate Model with thermosphere extension (WACCM-X) simulations. The geopotential height amplitude of wave 1 at 60°N and 1 hPa for the same time periods (d-f). (a-b) and (d-e) The solid lines are daily values, and the dotted lines are climatological values from the 20 years of simulation (see text for details), (c) and (f) The solid lines are monthly mean values, and the dashed lines are daily values.

Figure 2. Temperature at 90°S and 10 hPa of (a) first year and (b) 20 years of WACCM-X simulations. The geopotential height amplitude of wave 1 at 60°N and 1 hPa for the same time periods (c-d). (a) and (c) The solid lines are daily values, and the dotted lines are climatological values from the 20 years of simulation (see text for details). (b) and (d) The solid lines are monthly mean values, and the dashed lines are daily values.

Figure 3. Similar to Figure 1, but for diurnal westward propagating wave 1 (DW1) at 20°N and semidiurnal westward propagating wave 2 (SW2) at 52°N, both at 10−4 hPa. (c) and (f) The dark dashed lines are the equatorial zonal mean zonal wind at 30